CrystEngComm

COMMUNICATION

View Article Online
View Journal | View Issue

Cite this: *CrystEngComm*, 2019, **21**, 5862

Received 18th June 2019,
Accepted 2nd September 2019

DOI: 10.1039/c9ce00944b

rsc.li/crystengcomm

Trinuclear Ni(II) oriented highly dense packing and π-conjugation degree of metal–organic frameworks for efficient water oxidation†

Zhi-Min Zhai,[ab] Xiao-Gang Yang,*[b] Zhao-Tong Yang,[b] Xiao-Min Lu[b] and Lu-Fang Ma[ab]

Oriented by the structure-directing effect of metal clusters, a novel trinuclear nickel-based MOF (Ni–BTC) exhibited highly denser crystal packing and π-conjugation degree, providing a platform for efficient charge carrier mobility between metal clusters through π-conjugated molecular bridges and long-term stability of an efficient oxygen evolution reaction.

1. Introduction

With the rapid development of economy, the problems of environmental pollution and energy crisis are becoming more and more serious. Therefore, developing sustainable clean energy to solve the problems has become a hot spot of scientific research.[1,2] In this case, the electrochemical splitting of water molecules to produce hydrogen and oxygen is considered as a viable green path. The water splitting reaction occurs through two half-cell reactions: hydrogen evolution reaction (HER) and oxygen evolution reaction (OER).[3] OER is the key half reaction for water splitting.[4–8] However, owing to the sluggish kinetics of OER, there is a need to search for an efficient electrocatalyst that can overcome the kinetic barriers and expedite the reaction.[9–11] At present, the electrocatalysts with the best catalytic performance are still noble metals.[12–14] Nevertheless, high cost, scarcity and poor stability have limited their further development in electrocatalytic reactions. Therefore, it is significant to find a green and clean electrocatalyst with high catalytic efficiency, high stability and low cost.[15–18]

Metal–organic frameworks (MOFs) are crystalline materials with self-assembled metal ions/clusters with organic ligands and they have been well studied. Benefiting from the high specific surface area, structural diversity and functional properties,[19–25] MOFs have been widely used for various aspects such as catalysts,[26–28] sensors,[29–33] and optical waveguides[34–39] Theoretically, MOFs can be designed as a category of promising candidates for electrocatalysts with high catalytic efficiency by using different metal ions/clusters and ligands. Moreover, the porous structure of MOFs can offer a high internal surface area and high concentration of catalytic sites and increase the contact area between the electrolyte and the electrocatalyst, thus improving the catalytic activity more effectively. Unfortunately, there are very few reports about MOFs as electrocatalysts, especially for applications in OER.[40] The greatest challenge that currently exists is the intrinsic electronic conductivity and the long-term stability of MOFs. Although efforts have already been made to promote the electrocatalytic performance of MOFs, a general and efficient approach for tuning the component and structure of MOFs on the molecular scale is still needed. Based on the above considerations, herein, a trinuclear nickel-based MOF $[Ni_3(BTC)_2(H_2O)_8]$ (H_3BTC = 1,3,5-trimesic acid, Ni–BTC) was synthesized under solvothermal conditions and its crystal structure was determined by single-crystal X-ray diffraction. Oriented by the trinuclear Ni(II) cluster, Ni–BTC exhibited highly dense crystal packing and π-conjugation degree, providing long-term stability and efficient electron transfer between metal clusters. The electrocatalytic measurements revealed that Ni–BTC MOF showed high efficiency for OER with a lower overpotential of only 270 mV at 10 mA cm^{-2} as well as long-term water electrolysis at a constant potential for 48 h.

2. Experimental

2.1 Characterization

Single-crystal X-ray diffraction data for Ni–BTC were recorded at room temperature on an Oxford Diffraction SuperNova area-detector diffractometer using mirror optics

[a] *College of Chemistry and Molecular Engineering, Zhengzhou University, Zhengzhou 450001, P. R. China*
[b] *College of Chemistry and Chemical Engineering, Henan Province Function-Oriented Porous Materials Key Laboratory, Luoyang Normal University, Luoyang 471934, P. R. China. E-mail: yxg2233@126.com*

† Electronic supplementary information (ESI) available. CCDC 1933076. For ESI and crystallographic data in CIF or other electronic format see DOI: 10.1039/c9ce00944b

monochromated Mo Kα radiation (λ = 0.71073 Å). CrysAlisPro[41] was used for the data collection, data reduction and empirical absorption correction. The crystal structure was solved by direct methods using SHELXS-2014 and least-squares refined with SHELXL-2014 using anisotropic thermal displacement parameters for all non-hydrogen atoms.[42] The crystallographic data and selected bond parameters for Ni–BTC are listed in Tables S1 and S2.† CCDC no. 1933076 contains the supplementary crystallographic data for Ni–BTC. PXRD patterns were collected on a Bruker D8-ADVANCE X-ray diffractometer using Cu Kα radiation (λ = 1.5418 Å). Measurements were made in a 2θ range of 5–50° at room temperature with a step of 0.02° (2θ) and a counting time of 0.2 s per step. The operating power was 40 kV, 40 mA. Thermogravimetric analysis (TGA) experiments were carried out using an SII EXStar6000 TG/DTA6300 thermal analyzer from room temperature to 800 °C under a nitrogen atmosphere at a heating rate of 10 °C min^{-1}. The C, H analyses were carried out using a Perkin–Elmer Elementar vario elemental analysis instrument. The IR spectra were recorded in the range of 4000–400 cm^{-1} on a Nicolet 6700 (Thermo) FT-IR spectrometer with KBr pellets. The morphology of Ni–BTC powder was investigated using a field emission scanning electron microscope (SEM Sigma 500). Electrocatalytic measurements were recorded with a CHI 660E electrochemical analyzer (CH Instruments, Chenhua Co., Shanghai, China) in a standard three-electrode system using Ni–BTC powder-modified foam nickel as the working electrode with a working area of 1.0 cm^2, a platinum wire electrode as the counter electrode, and Ag/AgCl as the reference electrode; a 0.1 M KOH solution was used as the electrolyte. All electrochemical tests were performed at room temperature. The *iR* correction was performed by the electrochemical workstation automatically. Before the electrochemical measurements, the reference electrode was calibrated by performing cyclic voltammetry (CV) scans with a scan rate of 50 mV s^{-1} in nitrogen-saturated electrolytes. The linear-sweep voltammograms (LSV) were measured with a scan rate of 50 mV s^{-1}. All the potentials in this work were referenced to a reversible hydrogen electrode (RHE) according to $E(\text{RHE}) = E(\text{SCE}) + 0.197 + 0.059\ \text{pH}$.

2.2 Synthesis of Ni–BTC crystals

A mixture of trimesic acid (BTC, 0.5 mmol, 105 mg), $NiCl_2 \cdot 6H_2O$ (1 mmol, 237.6 mg), acetonitrile (2 mL) and H_2O (6 mL) was placed in a Teflon-lined stainless steel vessel, heated to 150 °C for 3 days, and then cooled to room temperature over 24 h. Light green block crystals of Ni–BTC were obtained. Elemental analysis: calc. (%) for $C_{18}H_{22}Ni_3O_{20}$: C, 29.44; H, 3.02; found (%): C, 30.89; H, 3.85.

2.3 Preparation of working electrode

The as-synthesized Ni–BTC crystals (10 mg) were grinded to powder and then mixed with polyvinylidene fluoride (PVDF, 5 mg) uniformly. Then, 0.2 mL DMF was added to the uniform mixture and gently stirred to form a homogeneous ink, which was covered onto the both sides of foam nickel (with a length of 4 cm and a width of 1 cm) and heated at 110 °C for about 1 hour.

3. Results and discussion

Ni–BTC in the crystal state was facilely synthesized under solvothermal conditions. The crystal structure and phase purity were further determined by single-crystal X-ray diffraction (Tables S1 and S2†) and powder X-ray diffraction analyses (PXRD, Fig. S1†). The PXRD pattern shows that all the diffraction peaks are identical and agree well with the simulated ones. This means that the Ni–BTC sample has high phase purity. Thermogravimetric analysis (Fig. S2†) revealed a weight loss of 19.9% up to about 280 °C, corresponding to the loss of coordinated water molecules (calcd 19.6%). The optical microscopy image (Fig. S3†) clearly shows similar morphologies of Ni–BTC. There are characteristic vibrations in the FT-IR spectra (Fig. S4†).

Single-crystal X-ray diffraction analysis revealed that Ni–BTC crystallized in the triclinic system with the $P\bar{1}$ space group, showing a trinuclear Ni(II)-based 3D network. As shown in Fig. 1a, all the Ni(II) ions are six-coordinated, but they have different coordination modes. Ni1 is in octahedral coordination geometry with five carboxylic oxygen atoms from five different BTC ligands and one H_2O molecule. The Ni2 and Ni4 centers are coordinated with two carboxylic oxygen atoms from two different BTC ligands and four H_2O molecules. The Ni3 center is coordinated with four carboxylic oxygen atoms from four different BTC ligands and two H_2O molecules. In Ni–BTC, each BTC ligand connects four Ni(II) ions through one bidentate and

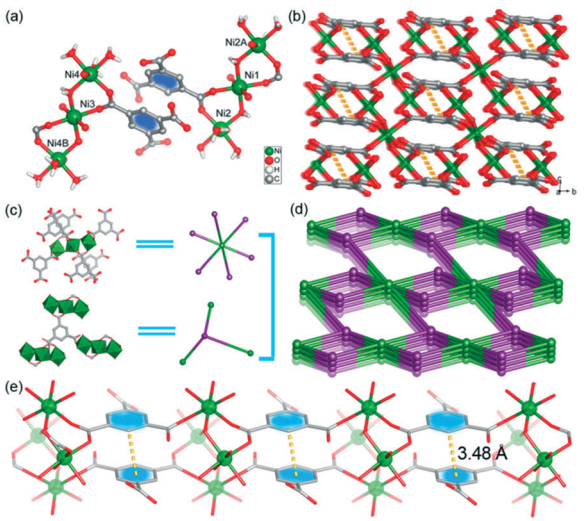

Fig. 1 (a) Coordination environment of Ni(II) ions in Ni–BTC. Symmetry codes: A: −x + 2, −y + 2, −z; B: −x + 1, −y, −z + 1. (b) View of the 3D network of Ni–BTC along the [100] direction. Schematic views of the 6-connected three trinuclear Ni(II) nodes and 3-connected BTC nodes (c) as well as the overall (3,6)-connected topology of Ni–BTC (d). (e) Arrangement of π···π stacking between benzene rings of BTC ligand molecules fixed by three trinuclear Ni(II) clusters.

two monodentate carboxylate groups. The dihedral angles between the benzene ring and three carboxylate groups in Ni–BTC are 13.51, 37.85 and 6.32°, indicating twisted conformation for the BTC ligand. Two bidentate carboxylate groups and two μ_2-H_2O link three Ni(II) ions to form two kinds of linear trinuclear Ni(II) units with the adjacent Ni···Ni distances of 3.592 Å and 3.622 Å, respectively. Based on the connection mode mentioned above, the trinuclear Ni(II) units are joined together to generate a 3D network (Fig. 1b). A better insight into the 3D network of Ni–BTC can be achieved by the application of the topological approach. Each trinuclear Ni(II) cluster can be viewed as a 6-connected node considering it bridges six BTC ligands, and each BTC ligand can be assumed as a 3-connected node because it coordinates to three trinuclear Ni(II) clusters (Fig. 1c). Thus, the 3D network of Ni–BTC MOF constructed by organic BTC nodes and inorganic trinuclear Ni(II) nodes can be simplified as (3,6)-connected topology (Fig. 1d).

Unlike mononuclear nodes, the rigid metal clusters play a significant role in the assembly of ordered frameworks, which usually hold more directional information by predestined bridging ligands and then control the overall coordination networks. Herein, the BTC ligands were tightly fixed between the linear trinuclear Ni(II) units through coordination bonds. Three carboxylate groups of the BTC ligand were forced to adjust its conformation, rotating outside the benzene ring plane to coordinate with the Ni(II) ions. In contrast, the benzene rings of the BTC ligand displayed a parallel packing mode with strong π···π (3.48 Å between the centroid of benzene rings) stacking interactions (Fig. 1b and e and S5†). The calculated BTC concentration[43] of 5.93 mol dm^{-3} suggested that the Ni–BTC MOF system can provide a more π-conjugation degree and highly dense crystal packing. From the analysis of the crystal structure, it can be predicted that the aromatic rings of the BTC ligand anchored between the trinuclear Ni(II) units can provide a platform for efficient free electron transfer from one metal cluster to the adjacent one along the π bonds in the π-conjugated molecular bridges. The highly dense crystal packing endowed Ni–BTC with higher physicochemical stability. In addition, abundant coordinated water molecules on the two sides of the linear trinuclear Ni(II) units could afford more chance for efficient OER.

To confirm the above prediction, the chemical stability of Ni–BTC was first tested in an electrolyte. The PXRD patterns (Fig. S6†) reveal that the crystal structure of Ni–BTC remains unchanged after soaking in a 0.1 M KOH aqueous solution for 48 h, indicating high stability of Ni–BTC in a basic electrolyte for further electrocatalytic measurements. Furthermore, the SEM image (Fig. 2a) clearly demonstrates the uniform nano-scale morphologies of Ni–BTC. Fig. 2b and S7† show the CV curve of Ni–BTC at a scan rate of 50 mV s^{-1} after 50 cycles. Pairs of reversible redox peaks (1.31 and 1.47 V) can be observed, suggesting that Ni–BTC is electrochemically active, and the electron transfer in the electrode reaction is quasi-reversible.

Linear sweep voltammetry (LSV) was performed in a 0.1 M KOH solution and all electrode potentials were expressed in reference to the reversible hydrogen electrode (RHE). It can be observed that the blank nickel foam working electrode needs a high overpotential of 590 mV at 10 mA cm^{-2}. In contrast, Ni–BTC exhibits significant enhancement of the electro-catalytic performance with the initial overpotential of 170 mV and overpotential of 270 mV at 10 mA cm^{-2} (Fig. 3a). By comparison of the catalytic ability with the previous results (Table 1), Ni–BTC shows a comparable OER performance with that of the reported MOF-based electrocatalysts in a basic electrolyte.

To further study the underlying electrocatalytic mechanism for OER, the corresponding Tafel plots based on the LSV curves are presented (Fig. 3b). Remarkably, the Tafel slope for Ni–BTC (120.7 mV dec^{-1}) is lower than that for the nickel foam (153.4 mV dec^{-1}), which is probably owing to the large contact surface and efficient charge transport. In addition, electrochemical impedance spectroscopy (EIS) analysis was performed to gain further insights into the activity of Ni–BTC-modified electrodes toward OER (Fig. 3c). Obviously, the

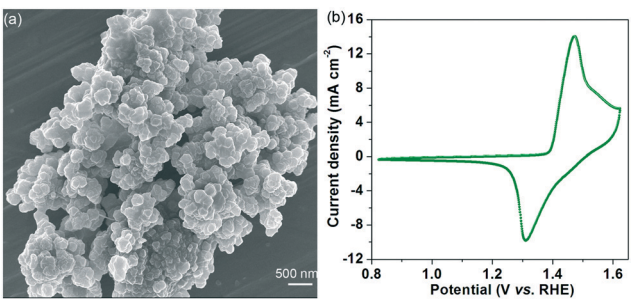

Fig. 2 SEM image (a) and cyclic voltammogram of Ni–BTC (b).

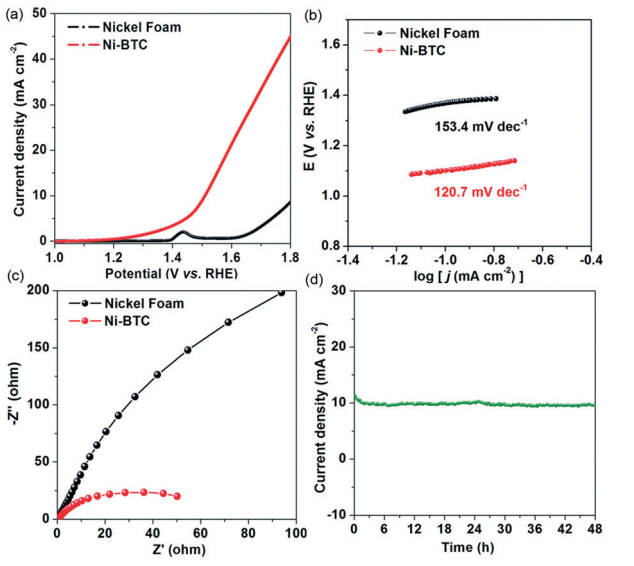

Fig. 3 The polarization curves (a), corresponding Tafel slope (b) and EIS Nyquist plots (c) of Ni–BTC and blank nickel foam tested in 0.1 M KOH. (d) Chronopotentiometry curves of Ni–BTC at the current density of 10 mA cm^2.

Table 1 Comparison of the OER activities of recently reported MOF-based catalysts in alkaline conditions

Catalysts	η_{10} (mV)	Substrate	Ref.
Ni–BTC	270	Foam nickel	This work
Ni-CP	356	Glassy carbon	1
NNU-23	365	Carbon cloth	44
UTSA-16	408	Glassy carbon	45
Fe_3–Co_2	237	Foam copper	46
Fe_3–Co_2	225	Foam nickel	46
FeTPyP–Co	351@1 mA cm^{-2}	Au	47
CTGU-14	454	Glassy carbon	48

charge transfer resistance (R_{ct}) of Ni–BTC was significantly lower than that of the nickel foam. This result indicates that Ni–BTC has a fast charge transfer rate to enhance the electrocatalytic performance for OER. The long-term time-dependent current density curve of Ni–BTC was also evaluated under the potential of 270 mV for 48 h. As shown in Fig. 3d, it can be easily observed that the current density exhibits negligible deterioration. The additional PXRD patterns, SEM image (Fig. S8†) and CV curves (Fig. S9†) after long-term OER suggest the good stability of the Ni–BTC electrode.

In summary, a novel Ni(II)-based MOF $[Ni_3(BTC)_2(H_2O)_8]$ (H_3BTC = 1,3,5-trimesic acid, Ni–BTC) was synthesized under solvothermal conditions. The formation of trinuclear nickel clusters played an essential role in affecting the molecular conformation and packing mode of the ligand, resulting in highly dense crystal packing and π-conjugation degree of the structure. This further provided a platform for efficient free electron transfer between metal clusters through the π bonds in the π-conjugated molecular bridges. As expected, the as-synthesized Ni–BTC electrochemical catalyst featured outstanding catalytic ability for OER with an overpotential of 270 mV at 10 mA cm^{-2} as well as long-term water electrolysis at a constant potential for 48 h in 0.1 M KOH. Therefore, this work will open up an effective way to develop highly active OER non-noble metal catalysts at the molecular scale.

Conflicts of interest

There are no conflicts to declare.

Acknowledgements

This work was supported by the National Natural Science Foundation of China (Grant No. 21771097).

Notes and references

1 C.-L. Wang, C.-Q. Song, W.-H. Shen, Y.-Y. Qi, Y. Xue, Y.-C. Shi, H. Yu and L. Feng, *Catal. Sci. Technol.*, 2019, **9**, 1769–1773.
2 M. B. Solomon, T. L. Church and D. M. D'Alessandro, *CrystEngComm*, 2017, **19**, 4049–4065.
3 P. K. Katkar, S. J. Marje, S. B. Kale, A. C. Lokhande, C. D. Lokhandem and U. M. Patil, *CrystEngComm*, 2019, **21**, 884–893.
4 Z. W. Seh, J. Kibsgaard, C. F. Dickens, I. Chorkendorff, J. K. Nørskov and T. F. Jaramillo, *Science*, 2017, **355**, 6321–6332.
5 Q. Zhao, Z. Yan, C. Chen and J. Chen, *Chem. Rev.*, 2017, **117**, 10121–10211.
6 B. Zhao, L. Zhang, D. Zhen, S. Yoo, Y. Ding, D. Chen, Y. Chen, Q. Zhang, B. Doyle, X. Xiong and M. Liu, *Nat. Commun.*, 2017, **8**, 14586.
7 X. Zheng, B. Zhang, P. De Luna, Y. Liang, R. Comin, O. Voznyy, L. Han, F. P. García de Arquer, M. Liu, C. T. Dinh, T. Regier, J. J. Dynes, S. He, H. L. Xin, H. Peng, D. Prendergast, X. Du and E. H. Sargent, *Nat. Chem.*, 2017, **10**, 149–154.
8 D. Guo, F. Chen, W. Zhang and R. Cao, *Sci. Bull.*, 2017, **62**, 626–632.
9 Y. Zhao, R. Nakamura, K. Kamiya, S. Nakanishi and K. Hashimoto, *Nat. Commun.*, 2013, **4**, 2390.
10 J. Suntivich, K. J. May, H. A. Gasteiger, J. B. Goodenough and Y. Shao-Horn, *Science*, 2011, **334**, 1383–1385.
11 P. Wang, M. Yan, J. Meng, G. Jiang, L. Qu, X. Pan, J. Z. Liu and L. Mai, *Nat. Commun.*, 2017, **8**, 645.
12 R. Subbaraman, D. Tripkovic, D. Strmcnik, K. C. Chang, M. U. Chimura, A. P. Paulikas, V. Stamenkovic and N. M. Markovic, *Science*, 2011, **334**, 1256–1260.
13 I. E. L. Stephens and I. Chorkendorff, *Angew. Chem., Int. Ed.*, 2011, **50**, 1476–1477.
14 J. Lai and S. Guo, *Small*, 2017, **13**, 1702156.
15 V. Artero and M. Fontecave, *Chem. Soc. Rev.*, 2013, **42**, 2338–2356.
16 M. W. Kanan and D. G. Nocera, *Science*, 2008, **321**, 1072–1075.
17 Y. Surendranath, D. A. Lutterman, Y. Liu and D. G. Nocera, *J. Am. Chem. Soc.*, 2012, **134**, 6326–6336.
18 L. He, J. Liu, Y. Liu, B. Cui, B. Hu, M. Wang, K. Tian, Y. Song, S. Wu, Z. Zhang, Z. Peng and M. Du, *Appl. Catal., B*, 2019, **248**, 366–379.
19 W. P. Lustig, S. Mukherjee, N. D. Rudd, A. V. Desai, J. Li and S. K. Ghosh, *Chem. Soc. Rev.*, 2017, **46**, 3242–3285.
20 Y. X. Tan, F. Wang and J. Zhang, *Chem. Soc. Rev.*, 2018, **47**, 2130–2144.
21 J. Zhou and B. Wang, *Chem. Soc. Rev.*, 2017, **46**, 6927–6945.
22 J. Liu, T. Y. Bao, X. Y. Yang, P. P. Zhu, L. H. Wu, J. Q. Sha, L. Zhang, L. Z. Dong, X. L. Cao and Y. Q. Lan, *Chem. Commun.*, 2017, **53**, 7804–7807.
23 R. W. Huang, Y. S. Wei, X. Y. Dong, X. H. Wu, C. X. Du, S. Q. Zang and T. C. W. Mak, *Nat. Chem.*, 2017, **9**, 689–697.
24 Q. Yang, Q. Xu and H. L. Jiang, *Chem. Soc. Rev.*, 2017, **46**, 4774–4808.
25 C.-S. Liu, Z.-H. Zhang, M. Chen, H. Zhao, F.-H. Duan, D.-M. Chen, M.-H. Wang, S. Zhang and M. Du, *Chem. Commun.*, 2017, **53**, 3941–3944.
26 X.-K. Wang, J. Liu, L. Zhang, L.-Z. Dong, S.-L. Li, Y.-H. Kan, D.-S. Li and Y.-Q. Lan, *ACS Catal.*, 2019, **9**, 1726–1732.
27 Y.-P. Wu, W. Zhou, J. Zhao, W.-W. Dong, Y.-Q. Lan, D.-S. Li, C. Sun and X. Bu, *Angew. Chem., Int. Ed.*, 2017, **56**, 13001–13005.

28 D. Shi, R. Zheng, M.-J. Sun, X. Cao, C.-X. Sun, C.-J. Cui, C.-S. Liu, J. Zhao and M. Du, *Angew. Chem., Int. Ed.*, 2017, **56**, 14637–14641.
29 D.-M. Chen, C.-X. Sun, Y. Peng, N.-N. Zhang, H.-H. Si, C.-S. Liu and M. Du, *Sens. Actuators, B*, 2018, **265**, 104–109.
30 W. H. Yin, Y. Y. Xiong, H. Q. Wu, Y. Tao, L. X. Yang, J. Q. Li, X. L. Tong and F. Luo, *Inorg. Chem.*, 2018, **57**, 8722–8725.
31 Y.-P. Li, S.-N. Li, Y.-C. Jiang, M.-C. Hu and Q.-G. Zhai, *Chem. Commun.*, 2018, **54**, 9789–9792.
32 M. B. Luo, Y. Y. Xiong, H. Q. Wu, X. F. Feng, J. Q. Li and F. Luo, *Angew. Chem., Int. Ed.*, 2017, **56**, 16376–16379.
33 G.-W. Xu, Y.-P. Wu, W.-W. Dong, J. Zhao, X.-Q. Wu, D.-S. Li and Q. Zhang, *Small*, 2017, **13**, 1602996.
34 X. Yang, X. Lin, Y. Zhao, Y. S. Zhao and D. Yan, *Angew. Chem., Int. Ed.*, 2017, **56**, 7853–7857.
35 D.-M. Chen, J.-Y. Tian, Z.-W. Wang, C.-S. Liu, M. Chen and M. Du, *Chem. Commun.*, 2017, **53**, 10668–10671.
36 L.-L. Ma, Y.-Y. An, L.-Y. Sun, Y.-Y. Wang, F. E. Hahn and Y.-F. Han, *Angew. Chem., Int. Ed.*, 2019, **58**, 3986–3991.
37 M.-M. Gan, J.-Q. Liu, L. Zhang, Y.-Y. Wang, F. E. Hahn and Y.-F. Han, *Chem. Rev.*, 2018, **118**, 9587–9641.
38 S. J. Liu, S. D. Han, J. P. Zhao, J. Xu and X. H. Bu, *Coord. Chem. Rev.*, 2019, **394**, 39–52.
39 Q.-G. Zhai, X. Bu, X. Zhao, D.-S. Li and P. Feng, *Acc. Chem. Res.*, 2017, **50**, 407–417.
40 L. Li, J. He, Y. Wang, X. Lv, X. Gu, P. Dai, D. Liu and X. Zhao, *J. Mater. Chem. A*, 2019, **7**, 1964–1988.
41 G. M. Sheldrick, *Acta Crystallogr., Sect. A: Found. Crystallogr.*, 2008, **64**, 112–122.
42 G. M. Sheldrick, *Acta Crystallogr., Sect. A: Found. Adv.*, 2015, **71**, 3–8.
43 R. Liu, Q.-Y. Liu, R. Krishna, W. Wang, C.-T. He and Y.-L. Wang, *Inorg. Chem.*, 2019, **58**, 5089–5095.
44 X.-L. Wang, L.-Z. Dong, M. Qiao, Y.-J. Tang, J. Liu, Y. Li, S.-L. Li, J.-X. Su and Y.-Q. Lan, *Angew. Chem., Int. Ed.*, 2018, **57**, 9660–9664.
45 J. Jiang, L. Huang, X. Liu and L. Ai, *ACS Appl. Mater. Interfaces*, 2017, **9**, 7193–7201.
46 J.-Q. Shen, P.-Q. Liao, D.-D. Zhou, C.-T. He, J.-X. Wu, W.-X. Zhang, J.-P. Zhang and X.-M. Chen, *J. Am. Chem. Soc.*, 2017, **139**, 1778–1781.
47 B. Wurster, D. Grumelli, D. Hötger, R. Gutzler and K. Kern, *J. Am. Chem. Soc.*, 2016, **138**, 3623–3626.
48 J.-W. Tian, Y.-P. Wu, Y.-S. Li, J.-H. Wei, J.-W. Yi, S. Li, J. Zhao and D.-S. Li, *Inorg. Chem.*, 2019, **58**, 5837–5843.

